Hindawi
International Journal of Antennas and Propagation
Volume 2023, Article ID 8969565, 14 pages
https://doi.org/10.1155/2023/8969565

Research Article

A Flexible Wearable Antenna with Annular Solar Eclipse Structure for ISM/WLAN/WIMAX/Bluetooth Applications

Zhen Yu, Runzhi Sun, Guodong Zhang, Ruirong Niu, Xiaoying Ran, and Ziheng Lin

North China Institute of Science and Technology, Langfang 101601, China

Correspondence should be addressed to Xiaoying Ran; starsky202@ncist.edu.cn

Received 15 July 2023; Revised 25 August 2023; Accepted 21 September 2023; Published 4 October 2023

Academic Editor: Trushit Upadhyaya

This paper proposes a wearable flexible dual-band antenna that covers the 2.34–2.68 GHz and 4.05–5.26 GHz frequency bands. This antenna employs a novel nested imitation annular solar eclipse structure, where the main radiator is a gradually widening loop, and another loop is coupled inside the radiator. The antenna, with overall dimensions of $40 * 32 * 0.3\,mm^3$, utilizes polyimide as the dielectric material. The gain, efficiency, and cross-polarization of the antenna were tested using a microwave anechoic chamber. The antenna achieves a maximum gain of 6 dBi and a maximum efficiency of 79.6%. We tested the SAR of the antenna at 10 mm from the human body, which was significantly below the international standard of 2.0 W/kg. The flexible antenna presented in this paper exhibits a broad low-frequency bandwidth, enabling coverage of various communication bands such as ISM, WLAN, WIMAX, and Bluetooth. The antenna delivers satisfactory simulation and measurement results while meeting the requirements of minimizing radiation exposure to the human body.

1. Introduction

In recent years, due to the rapid development of society and the continuous innovation of science and technology, traditional flat electronic devices have been difficult to adapt to the current complex and changing environment. The rapid development of flexible electronic devices is becoming more and more popular. Flexible electronic devices have a certain degree of stretching and bending and can conform to any surface characteristics. In the field of wireless communication, they are becoming more and more widely used. The most central component of wireless communication is the antenna used to transmit and receive electromagnetic waves, and every year, many scientists are looking for various new flexible materials to replace conventional materials as the substrate of microstrip antennas in order to break through the antenna with high radiation stability while having large bending. In 2014, Prof. Song et al. [1] designed and fabricated rectangular microstrip antennas using polydimethylsiloxane (PDMS) injected with liquid eutectic gallium indium (EGaIn) as a substrate and measured their center frequency up to 3.4 GHz. Hussain et al. [2] fabricated a flexible wearable antenna by electroplating 4 μm copper (Cu) on polyimide (PI) in 2016, and the antenna was manufactured in an S-shape, and its center frequency was measured to be 2.45 GHz. In 2017, Yan et al. [3] sputtered a layer of metallic Ag with a thickness of 50 nm on PI film by magnetron sputtering technique, and when the antenna was stretched by 200%, its central frequency still reached 5.6 GHz. It has a series of advantages, such as being flexible, cheap, and reusable [4], so it is suitable to be chosen as the material for the preparation of highly stable flexible antennas. The combination of monopole antenna and SRR enables the antenna to cover multiple frequency bands [5]. The combination of microstrip gap and SRR plays a significant role in the design of miniaturized antennas for dual-band performance [6]. Coupling plays a vital role in antenna parameters such as impedance, bandwidth, and resonant frequency [7].

Future industries, including wearable devices, flexible microelectronic products, and flexible integrated circuits, have garnered significant attention from society due to their

potential for transformative impact and wide-ranging applications. The demand for flexible antennas and flexible passive devices has experienced a significant surge due to the need to develop wireless communication systems that can be seamlessly integrated into flexible materials. Various antenna designs based on different flexible materials such as liquid crystal polymers (LCP), polyetherimide (PEI), and polyethylene terephthalate (PET) have been proposed. These materials have unique RF properties, such as a low dielectric constant and loss tangent angle. Recently, polyimide has been widely used to make dielectric substrates for flexible devices because of its excellent mechanical and electrical properties. Therefore, in this paper, polyimide is chosen as the dielectric board for the involved antenna. Feasible antenna designs with flexible properties face problems such as excessive design size, low bending degree, and distortion of antenna performance due to bending [8–13], so it becomes especially important to study flexible antennas. In [14], a flexible planar monopole antenna with a circular coupling structure is proposed. The antenna is a toroidal structure based on third-iteration scaling and nesting. The antenna designed in this paper utilizes a bionic nested structure. Compared to [14], this double circular antenna structure is smaller in size and simpler in structure. This idea is derived from the natural phenomenon of an annular eclipse. This structure efficiently enhances the current path, thereby improving impedance matching and radiation characteristics in the desired frequency bands.

The performance comparison between the antenna proposed in this paper and the antenna in the reference is shown in Table 1. The antenna proposed in this paper employs a coplanar waveguide structure to achieve multiband, relatively high gain, and relatively high efficiency.

In this paper, a new nested bionic structure is proposed. The idea is derived from the natural phenomenon of an annular solar eclipse, as shown in Figure 1. A coplanar waveguide antenna is designed based on this unitary mechanism, which effectively increases the current path and improves the impedance matching and radiation characteristics in the target frequency band. Based on the relevant principles of coplanar waveguide antennas, a dual-band flexible antenna is designed in combination with multiband and miniaturization features. The broadband technology and miniaturization technology of coplanar waveguide antennas are also combined to slot the antenna on the basis of the Archimedean spiral structure [13], and the influence of parameters such as dielectric material and antenna structure on antenna parameters during the design of the flexible antenna is further explored on the basis of the basic theory and research methods of conventional antenna design.

The antenna dielectric material is polyimide, which is smaller in size and has flexible bending characteristics compared to traditional microstrip antennas, making it suitable for small smart terminals, especially for devices with more stringent size requirements such as smart watch antennas. The total size of the dual circular dual-band flexible antenna designed in this paper is $32 \times 40 \times 0.3\,\text{mm}^3$. Meanwhile, the antenna designed in this section has almost omnidirectional radiation pattern on the E and H planes, and the peak gain of the antenna can reach −22.26 dBi, −27.05 dBi, and −16.23 dBi, respectively, in the 2.489/4.189/4.967 GHz band, ISM2400 band, WLAN (2402–24835 MHz), WIMAX (2.3–2.7 GHz), Bluetooth (2402–2480 MHz), and Chinese mid-band 4800 MHz–5000 MHz multiple communication frequency bands, and the application range is relatively wide.

2. Characteristics of the Antenna Structure

When using 3D high-frequency simulation software to build the antenna model, first, we need to estimate the size of the antenna according to the frequency requirements, and then, according to the calculation results, the parameters will be optimized, and finally, the antenna model will be selected to meet the design requirements. The following is a brief introduction to the calculation of some initial dimensions of the microstrip antenna.

When designing the antenna, we first select the dielectric substrate and need to consider the dielectric constant of the dielectric plate and then combined with the antenna working frequency to estimate the size of the radiation patch. Assuming that the dielectric constant of the dielectric plate is ε_r, the operating frequency f of the rectangular microstrip antenna, with the following formula, can be designed to radiate the width of the patch W, that is,

$$\mathrm{W} = \frac{c}{2f}\left(\frac{\varepsilon r + 1}{2}\right)^{-(1/2)}, \tag{1}$$

where c is the speed of light. The length of the radiation patch is generally taken to be $\lambda_e/2$. λ_e is the wavelength of the guided wave within the medium, that is,

$$\lambda e = \frac{c}{2f\sqrt{\varepsilon e}}. \tag{2}$$

After taking into account the edge shortening effect, the actual radiant cell length L should be

$$L = \frac{c}{2f\sqrt{\varepsilon e}} - 2\Delta L, \tag{3}$$

where ε_e is the effective dielectric constant and ΔL is the equivalent radiation gap length, which can be calculated separately using the following equation:

$$\varepsilon e = \frac{\varepsilon r + 1}{2} + \frac{\varepsilon r - 1}{2}\left(1 + 12\frac{h}{w}\right)^{-(1/2)}, \tag{4}$$

$$\Delta L = 0.412h\frac{(\varepsilon_e + 0.3)(w/h + 0.264)}{(\varepsilon_e - 0.258)(w/h + 0.8)}. \tag{5}$$

The antenna is printed on a polyimide dielectric plate with a thickness of 0.3 mm, a dielectric substrate size of $32 \times 40\,\text{mm}^2$, a relative permittivity of 3.5, and a dielectric loss rate of 0.008. The antenna comprises a double circular patch fed using coplanar waveguides and a trapezoidal ground plate on either side of the feed line. The outer ring of the double ring radiating patch affects the resonant characteristics mainly at the low frequency of 2.489 GHz, while its inner ring radiating patch affects the resonant

Table 1: Performance comparison of the proposed antenna with recent pioneering state of arts.

Ref.	Size (mm^3)	Res. freq. (GHz)	Bandwidths (%)	Dielectric material
1	$37 * 37 * 1$	3.4	4.4	PDMS
6	$83 * 56 * 1.56$	2.47/3.55/5.55	14.61/5.42/5.40	FR4
7	—	1.13/2.47/2.74	2.1/2.81/2.09	FR4
8	$102 * 60 * 0.8$	2.4/4.1/5.4	40	FR4
Prop.	$40 * 32 * 0.3$	2.48/4.19/4.97	19/37	Polyimide

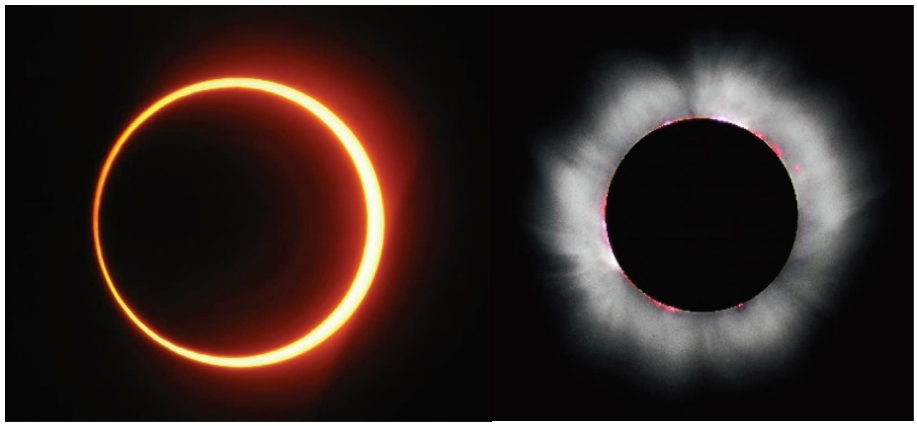

Figure 1: The annular solar eclipse.

characteristics mainly at the high frequencies of 4.189 GHz and 4.967 GHz. The trapezoidal ground plate on both sides of the feed line can effectively increase the high-frequency impedance bandwidth of the antenna. On the base model of the antenna in Figure 2, the antenna radiation patch, feed line width, and grounding plate are further optimized to obtain the final antenna structure diagram (Table 2).

The low-frequency bandwidth of the wearable flexible antenna designed in this paper can cover ISM2400 band, WLAN (2402–2483 MHz), WIMAX (2.3–2.7 GHz), and Bluetooth (2402–2480 MHz) multiple communication bands; its high-frequency bandwidth can cover the Chinese medium frequency band (4800 MHz–5000 MHz). The design is based on the theory of loop antenna and coplanar waveguide antenna, using equations (1) to (5) to calculate the preliminary rough data, and then, after HFSS simulation parameters optimization, to get the length of the dielectric plate $L = 32$ mm, width $W = 40$ mm, $H = 0.3$ mm, $R1 = 13$ mm, and $R2 = 12$ mm. At the same time, based on the advantages of coplanar waveguide compared to microstrip line feed, the antenna adopts the coplanar waveguide feeding method. Due to the broadband characteristics of coplanar waveguides, the antenna exhibits better robustness in frequency range when it is bent.

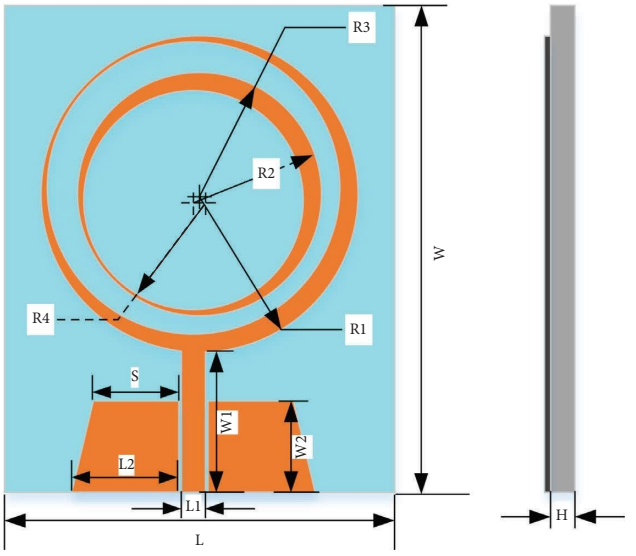

Figure 2: Antenna structure layout.

2.1. Simulation Results. The simulation was performed using the Ansoft High-Frequency Simulation Software (HFSS) (version 21.0). The evolution process of the wearable flexible antenna designed in this paper is described as follows: (i) the antenna shown in Figure 3, antenna *a*, was used as the basis, and after HFSS parameter scan optimization, the resonant frequency point of low frequency 2.489 GHz was obtained by changing the shape of its circular ring, and its structure is shown in Figure 3, antenna *b*. (ii) In order to increase its high-frequency characteristics, another circular ring was added, as shown in Figure 3, antenna *c*. (iii) By taking into account the coupling effect between the circular ring and the patch, the internal circular ring is scanned using HFSS to adjust the radius parameter and center position, resulting in the antenna configuration shown in Figure 3, which achieves desirable resonance frequencies of 4.189 GHz and 4.967 GHz at higher frequencies. (iv) At the same time, considering the narrower broadband, the grounding plate is broad banded so that the balance between antenna gain and bandwidth is obtained in Figure 3, antenna *e*. Through HFSS simulation analysis and parameter optimization, it

Table 2: The dimensions of the proposed antenna design.

Dimensions parameters	Unit (mm)
L	32
W	40
$L1$	2
$W1$	13
$L2$	8.8
$W2$	7.5
$R1$	13
$R2$	12
$R3$	10
$R4$	9
S	5.3

can be observed that the electrical parameters of antenna *e* align with the design requirements. Therefore, this design is considered as the final antenna structure, depicted as antenna *e* in Figure 3. The return loss of antenna a-antenna *e* is shown in Figure 4.

As shown in curve *e* in Figure 3, the designed antenna can operate in two different frequency bands: 2.4, 4.2, and 4.9 GHz at the center frequency point, with corresponding return loss of −22.26, −27.05, and −16.23 dB. The simulated −10 dB return loss bandwidth is 13% for the first frequency band (2.34–2.68 GHz) and 26% for the second band (4.05–5.26 GHz). The simulated −10 dB return loss bandwidth is 13% for the first frequency band (2.34–2.68 GHz) and 26% for the second band (4.05–5.26 GHz). This low-frequency bandwidth covers the ISM2400 band, WLAN (2402–24835 MHz), WIMAX (2.3–2.7 GHz), and Bluetooth (2402–2480 MHz), and the high-frequency bandwidth covers the Chinese mid-band (4800 MHz–5000 MHz).

The following is a discussion of the various important parameters affecting the performance of the antenna and to derive the optimal parameters. The characteristic impedance of a coplanar waveguide antenna without a metal ground plate on the back side is influenced by the transmission line width L1, ground plate, and thickness, so the influence of transmission line width L1, ground plate shape, and dielectric plate thickness on the return loss of the antenna is discussed here.

Figure 5 shows the comparison of the results of different return loss values from the feed line widths of 0.5 mm, 1 mm, 1.5 mm, and 2 mm by HFSS simulation. From the figure, it can be found that S11 has significant variations in all frequency bands at different widths. As the transmission line width increases, the entire frequency band shifts to the right, and with increasing width, the gain in the low-frequency band significantly increases. After comparing the different return loss values in Figure 5, it can be seen that the frequency band with $L1 = 2$ mm yields the best performance.

By comparing the different return loss values of rectangular and trapezoidal ground plates in HFSS simulation, Figure 6 shows that compared with rectangular ground plates, trapezoidal ground plates have higher gain and bandwidth in the low-frequency band and similar bandwidth but higher gain in the high-frequency band. Therefore, in the antenna design process, the shape and size of the ground plate can be changed appropriately, trying to achieve the best antenna performance with the best gain and bandwidth.

The bandwidth of the lower band for a dielectric substrate thickness H of 0.3 mm ranges from 2.34 to 2.68 GHz, for a total of 0.34 GHz. The bandwidth of the high band ranges from 4.05 to 5.26 GHz, for a total of 1.21 GHz. The bandwidth of the low-frequency band ranges from 2.30 to 2.65 GHz at a thickness H of 0.4 mm, for a total of 0.35 GHz. The bandwidth of the HF band ranges from 3.94 to 5.18 GHz, for a total of 1.24 GHz. The bandwidth ranges from 2.27 to 2.63 GHz at 0.5 mm thickness H for a total of 0.36 GHz at low frequencies. The bandwidth of the HF band ranges from 3.85 to 5.11 GHz, for a total of 1.26 GHz. As shown in the return loss comparison chart with different substrate thicknesses in Figure 7, it can be observed that as the substrate thickness increases, the return loss curve of the antenna's high-frequency band (4.05–5.26 GHz) shifts to the left, while the displacement range of the low-frequency band (2.34–2.68 GHz) is small and negligible; working bandwidth will increase with increase in the thickness of the antenna media substrate.

The current distribution and current vector direction on the antenna surface are shown in Figures 8(a)–8(c), respectively. As shown in Figure 8(a), at 2.489 GHz, the current is mainly distributed in the left and right sides of the feed line, close to the edge of the feed line grounding plate and the outside of the outer ring. Current through the feed line through the two ends of the outer ring flows to the top of the antenna radiation body, in the inner ring, the current from the feed point farther away from the end of the inner ring on both sides of the flow to the end of the feed point near, and then the grounding plate, the current from the two ends of the flow to the direction of the feed line, the overall direction tends to be parabolic. As can be seen from Figure 8(b), at 4.189 GHz, the current is mainly distributed on the left and right sides of the feeder, near the edge of the grounding plate of the feeder, and on the left side of the outer circular ring. From Figure 8(c), it can be seen that at 4.967 GHz, the current is mainly distributed in the lower half of the feeder, the left and right sides of the inner ring, and the edge of the grounding plate close to the feeder, with a small amount of current distributed on the left side of the outer ring.

The simulated 3D far-field radiation pattern and the far-field normalized E/H surface radiation pattern are shown in Figures 9 and 10. In Figure 10, the red solid line shows the main polarization at Phi = 0°, and the blue dashed line shows the cross-polarization at Phi = 90°. The peak gains are 2.5 dBi, 3.2 dBi, and 5.2 dBi at center frequencies of 2.489 GHz, 4.189 GHz, and 4.967 GHz, respectively. It can be clearly seen that this antenna has good radiation characteristics in the effective frequency band, with good omnidirectionality in the E and H planes and almost no zero point. This antenna has a small cross-polarization characteristic.

The antenna dielectric plate is a flexible material, and the antenna needs to be bent to different degrees in the HFSS software. The antenna is bent at different radii in the longitudinal direction to test the return loss value and radiation direction performance under different bending degrees. The structure of the antenna under three different bending radii

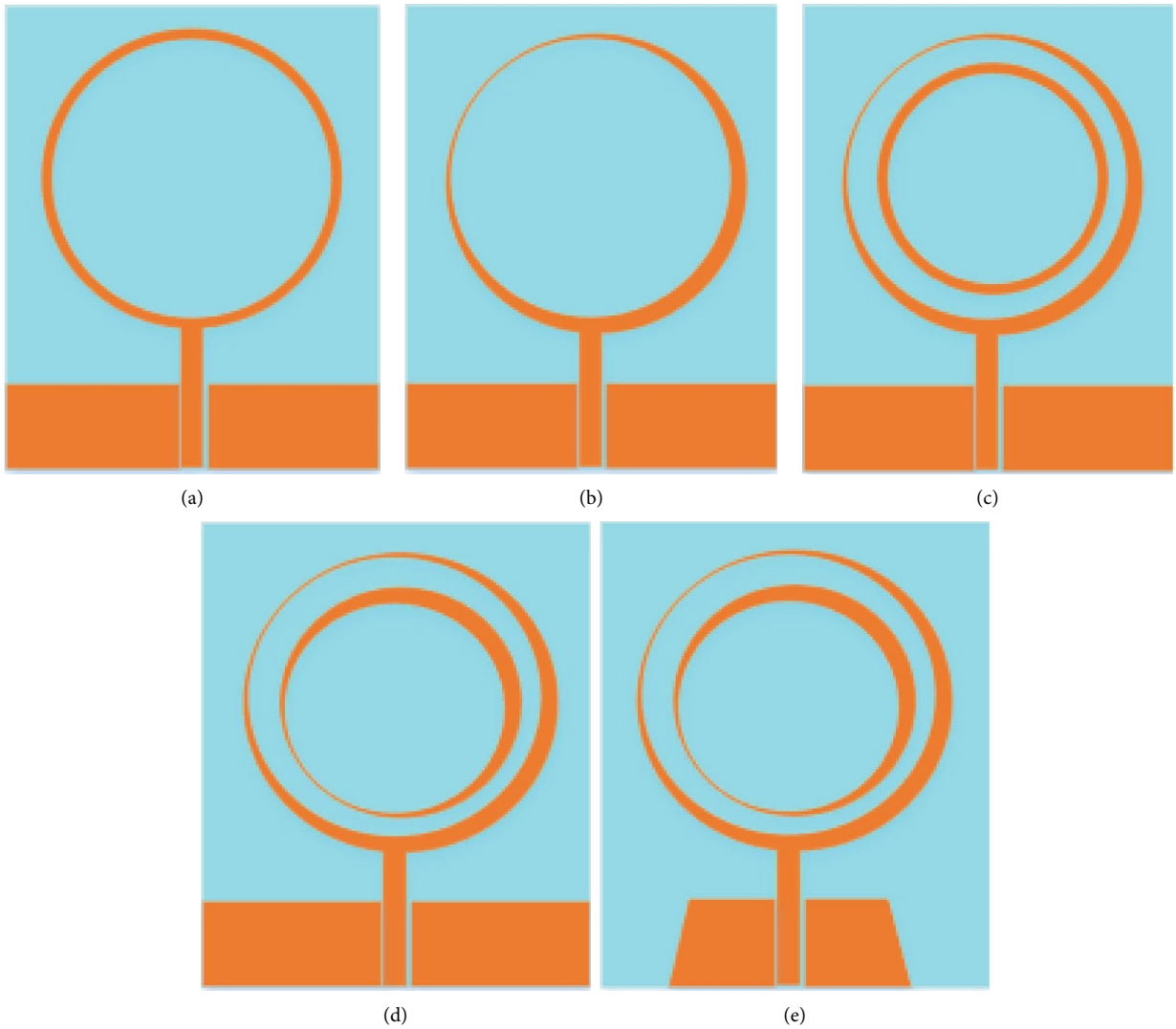

Figure 3: Antenna evolution process structure diagram.

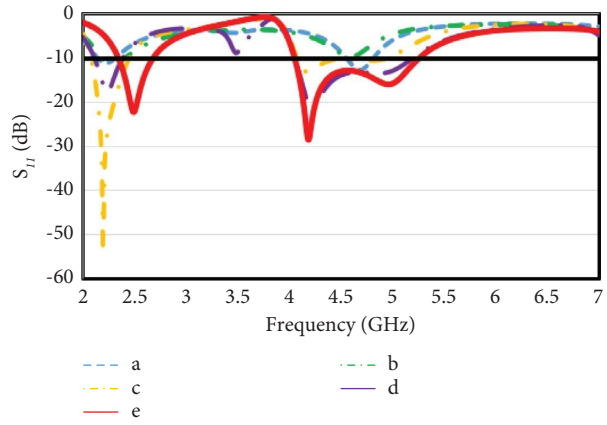

Figure 4: S11 comparison diagram of antenna iteration.

R towards the longitudinal axis is shown in Figure 11, with bending radii of $R = 30$ mm, $R = 40$ mm, and $R = 50$ mm, respectively.

The return loss of the antenna at different bending radii towards the longitudinal axis is shown in Figure 12. The return loss at bending radii of 30 mm, 40 mm, and 50 mm

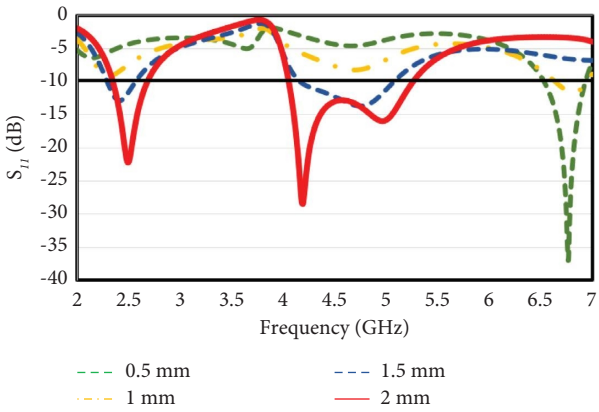

Figure 5: S11 comparison diagram of different transmission line widths.

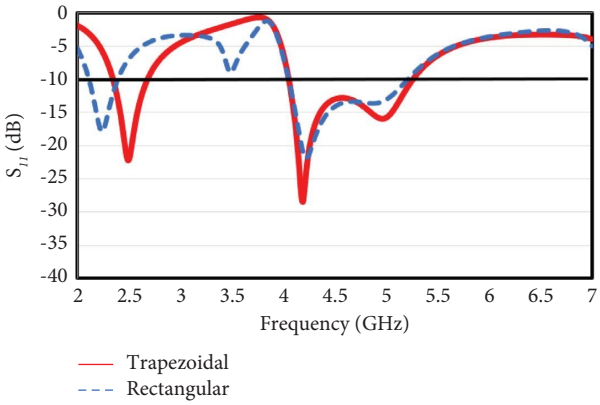

Figure 6: S11 comparison diagram of different flooring shapes.

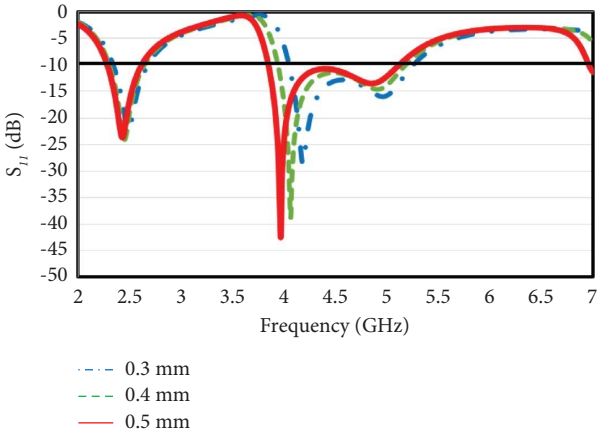

Figure 7: S11 comparison diagram of different media plate thicknesses.

shows no significant resonant frequency shift in the range of 2.34–2.68 GHz compared to the unbent return loss. When bent at different angles towards the vertical axis, the −10 dB bandwidth widens in the second frequency band and still meets the communication requirements well. The difference in return loss between the three different bending radii of the antenna is not significant. In summary, the antenna can meet its communication requirements well at different bending degrees.

The antenna is responsible for several commercial frequency bands used in wearable devices, such as Wi-Fi, WiMAX, and Bluetooth. Therefore, the antenna needs to be simulated for its radiation-specific absorption rate (SAR) values to the human body and its radiation direction performance when worn. The antenna will be moved through the axes to the arms of a human model drawn for simulation. The antenna will be placed 10 mm away from the human body and parallel to the arm, with clothing spaced from the human body, in accordance with an antenna bend radius of 30 mm. Three central frequency points in the antenna return loss, namely, 2.489 GHz, 4.189 GHz, and 4.967 GHz, were selected to test the SAR values of the antenna to see the absorption ratio of radiation by the human body. The simulated SAR values of the antenna at these frequencies are shown in Figure 13. The SAR value of the antenna at 2.489 GHz for the human arm is 0.7684 W/kg, at 4.189 GHz for the human arm is 0.8917 W/kg, and at 4.967 GHz for the human arm is 0.9563 W/kg. The human simulation SAR value graph shows that although the SAR value of the antenna increases as the resonant frequency point moves towards higher frequencies, the SAR value of the antenna is much lower than the international standard of 2.0 W/kg at 10 mm distance from the human body. The simulation shows that the antenna is suitable for wearable devices and will not cause radiation damage to the human body, which meets the requirement of minimum radiation exposure to the human body.

Figure 14 shows the radiation direction performance of the antenna after loading the human body. The gain at the three central frequency points of 2.489 GHz, 4.189 GHz, and 4.967 GHz are 1.6 dBi, 4.9 dBi, and 6.0 dBi, respectively. From the figure, it can be seen that when the antenna is worn on the human body, the main radiation direction is towards the front of the antenna. The radiation gain towards the human body is small, while the radiation gain towards the outside is large. In summary, the SAR values of the antenna to the human body are below the national standard, and the antenna has good directionality towards the human body. Therefore, it can be used as an antenna for wearable devices.

2.2. Fabrication and Measured Results. The antenna was fabricated and tested in a microwave darkroom to verify the correctness of the bandwidth, frequency, and performance of the design. The antenna was printed on a polyimide dielectric plate with a thickness of 0.3 mm, a dielectric plate size of $32 \times 40\,\text{mm}^2$, a relative permittivity of 3.5, and a dielectric loss rate of 0.008. Figure 15 shows the actual antenna and the experimental test setup.

A comparison between the measured S11 and simulated S11 of the antenna is shown in Figure 16. The first frequency point was moved from 2.49 GHz to 2.58 GHz with a return loss of −19.33 dB. The second frequency point was moved from 4.19 GHz to 4.34 GHz with a return loss of −17.82 dB. The third frequency point was moved from 4.98 GHz to

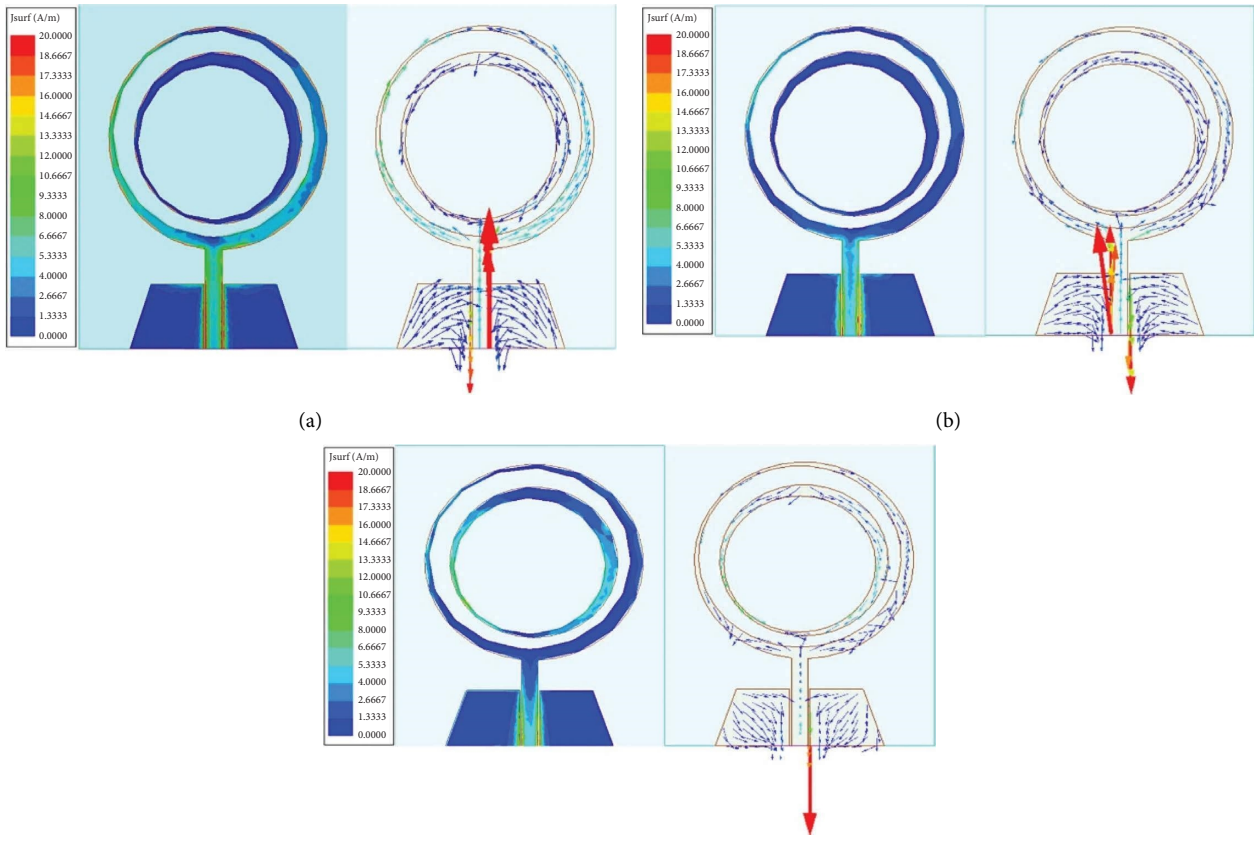

Figure 8: Current amplitude and vector distribution of the antenna at (a) 2.489 GHz, (b) 4.189 GHz, and (c) 4.967 GHz.

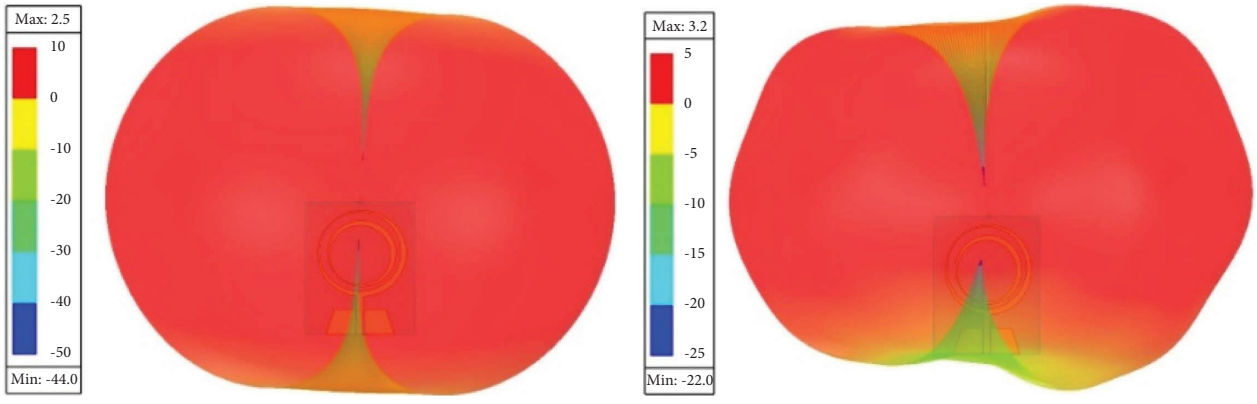

Figure 9: Continued.

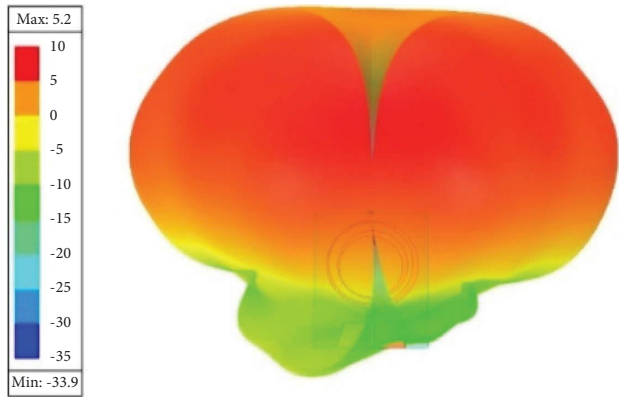

(c)

Figure 9: 3D radiation patterns at (a) 2.489 GHz, (b) 4.189 GHz, and (c) 4.967 GHz.

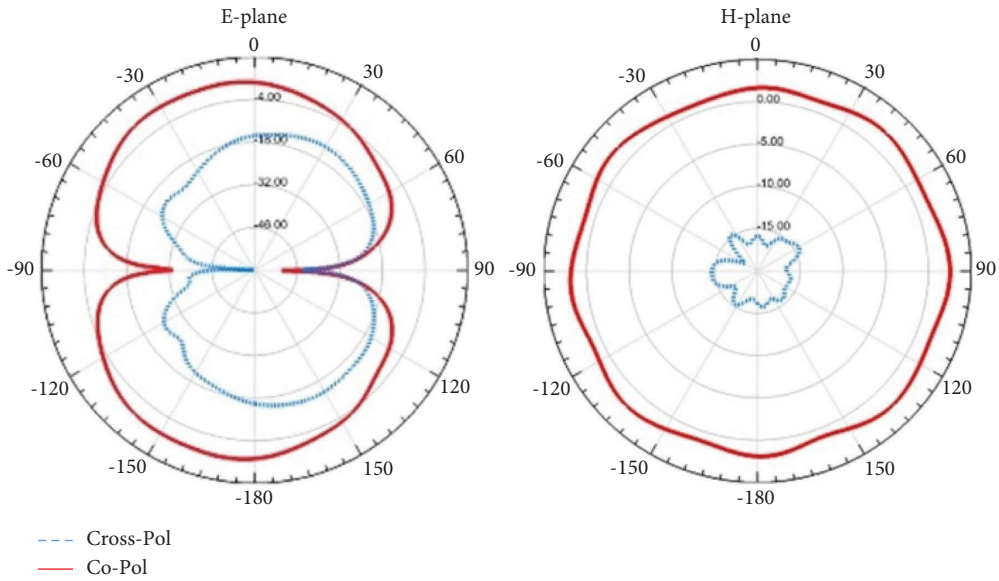

(a)

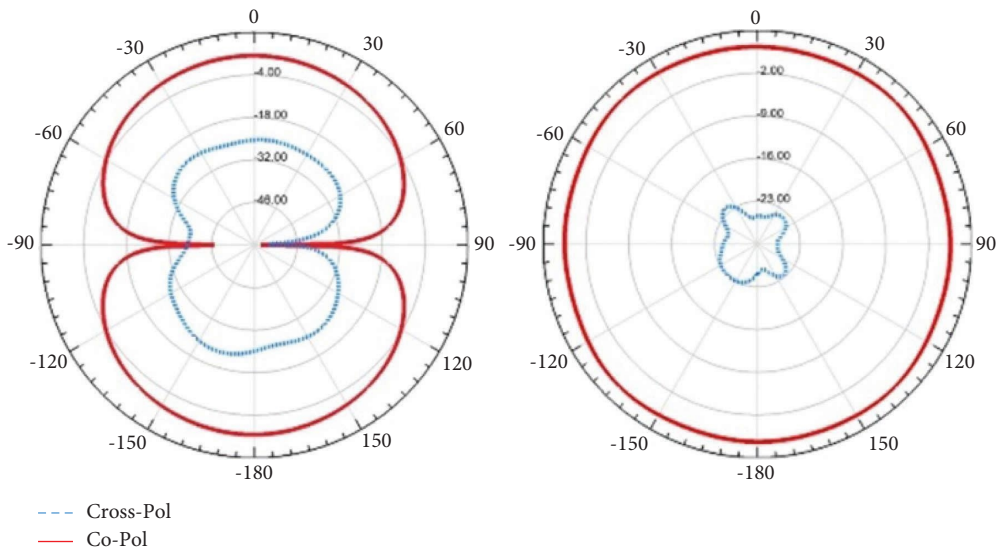

(b)

Figure 10: Continued.

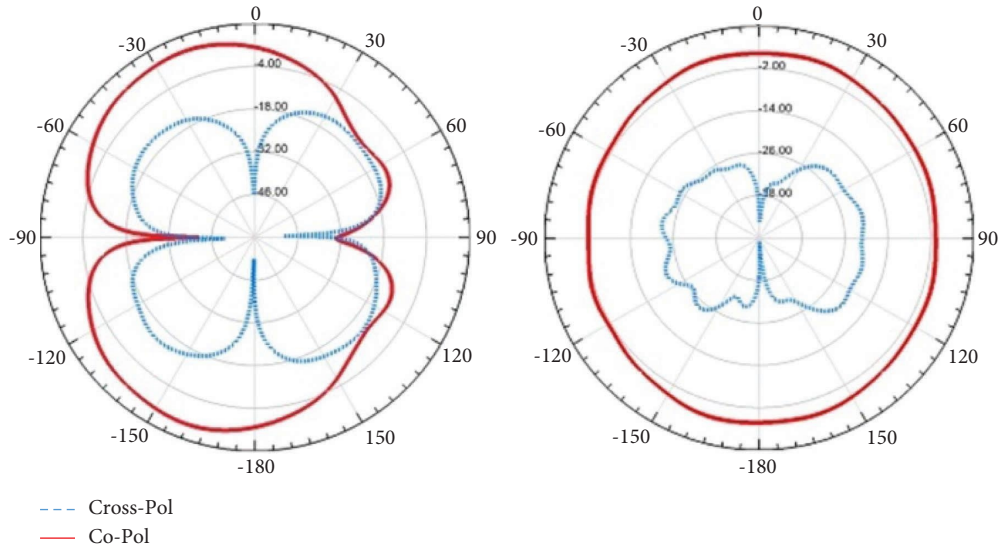

(c)

Figure 10: E/H plane radiation patterns at (a) 2.489 GHz, (b) 4.189 GHz, and (c) 4.967 GHz.

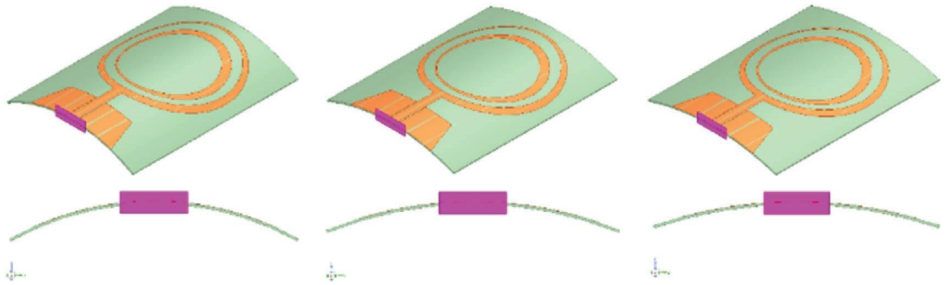

(a) (b) (c)

Figure 11: Schematic diagram of antenna bending towards Y-axis under different bending radii. (a) $R = 30$ mm. (b) $R = 40$ mm. (c) $R = 50$ mm.

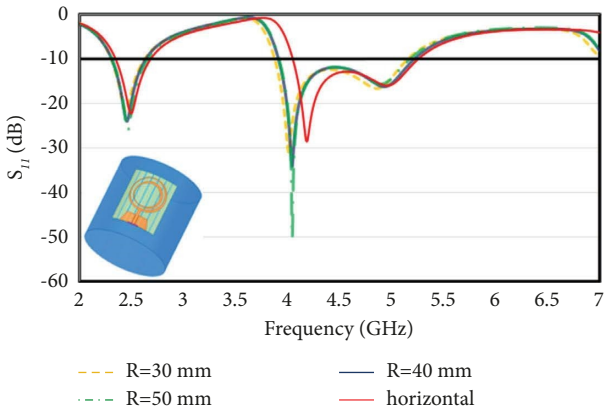

Figure 12: Comparison of return loss of antenna under different bending radii.

5.14 GHz with a return loss of −26.8915 dB. There are two frequency bands corresponding to the above frequency points. The first band (2.32 GHz–2.78 GHz) has a relative bandwidth of 19%. The relative bandwidth of the second band (4.14 GHz–6.05 GHz) is 37%.

The return loss of the antenna at different bending degrees is shown in Figure 17. The bandwidth of the low-frequency band changes less at different bending degrees. As the bending radius decreases, the bandwidth of the high-frequency band of the antenna increases, but it can still cover the required frequency range well. In summary, the different bending degrees have less effect on the return loss of the antenna.

Figures 18 and 19 show the 3D far-field radiation pattern of the antenna at each frequency point and the comparison diagram of the main polarization and cross-polarization of the E/H plane of the antenna, respectively. The measured and simulated results maintain a good agreement. The designed antenna shows very good radiation characteristics in all frequency bands, with omnidirectionality in the H plane. However, some discrepancies between the experimental and simulated data can also be found in this case, which are due to unavoidable errors caused by the external environment and the construction of the instrument during the actual measurement.

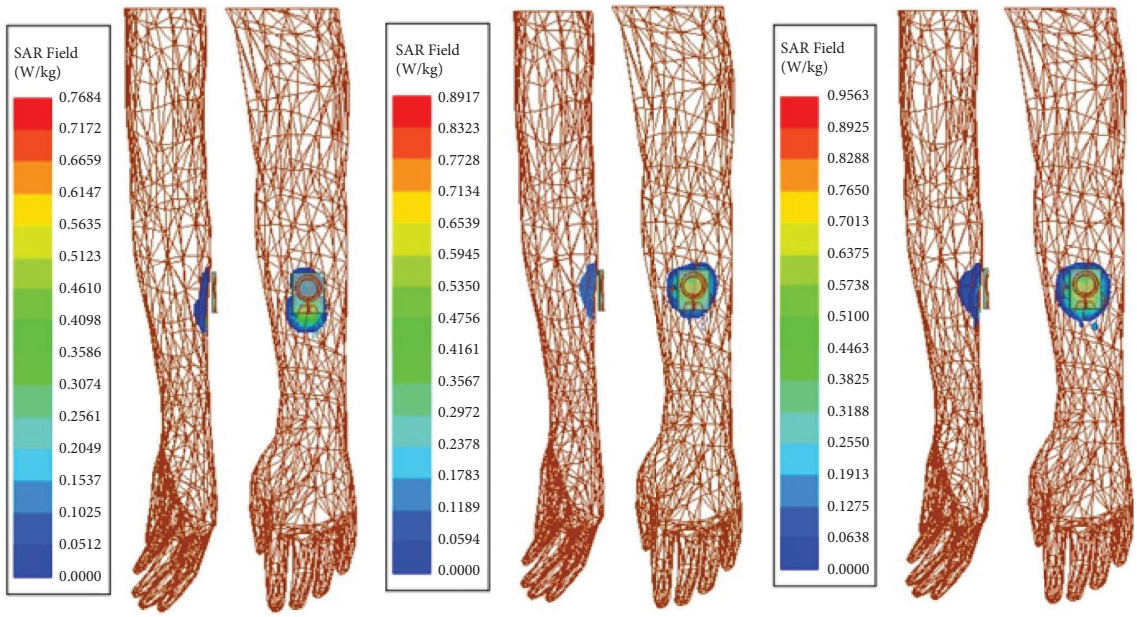

Figure 13: Simulated SAR value of antenna at (a) 2.489 GHz, (b) 4.189 GHz, and (c) 4.967 GHz.

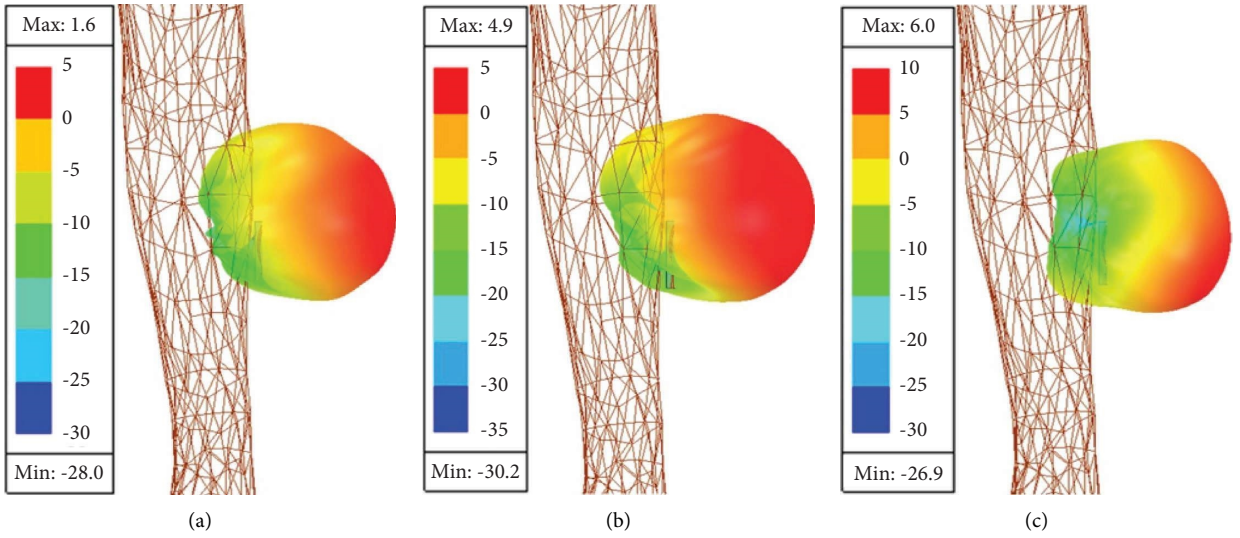

Figure 14: Antenna radiation direction after loading human body at (a) 2.489 GHz, (b) 4.189 GHz, and (c) 4.967 GHz.

The antenna designed for this occasion has two effective frequency bands: the first band (2.32GHz-2.78 GHz) and the second band (4.14 GHz–6.05 GHz). The gain of the actual antenna is shown in Figure 9. The peak gains are 2.5 dBi, 3.2 dBi, and 5.2 dBi at center frequencies of 2.489 GHz, 4.189 GHz, and 4.967 GHz. As can be seen from Figure 20, the antenna achieved a maximum gain of 6 dBi and a maximum efficiency of 79.6%. In the effective frequency band of the antenna, the gain range of the first band is 1.2–2.62 dBi and the efficiency range is 37.28%–52.85%. The second band has a gain range of 0.63–5.41 dBi and an efficiency range of 26.03%–79.41%. Compared to the simulated antenna's center frequency gain, the gain at the first frequency point decreased from 2.5 dBi to 1.97 dBi, the gain at the second frequency point increased from 3.2 dBi to 4.08 dBi, and the gain at the third frequency point decreased from 5.3 dBi to 2.06 dBi. The discrepancy may be attributed to the fact that the simulation process was conducted with ideal feed points and did not account for the losses caused by the SMA connector in the measurement process. However, the antenna still meets the requirements for the desired application frequency range.

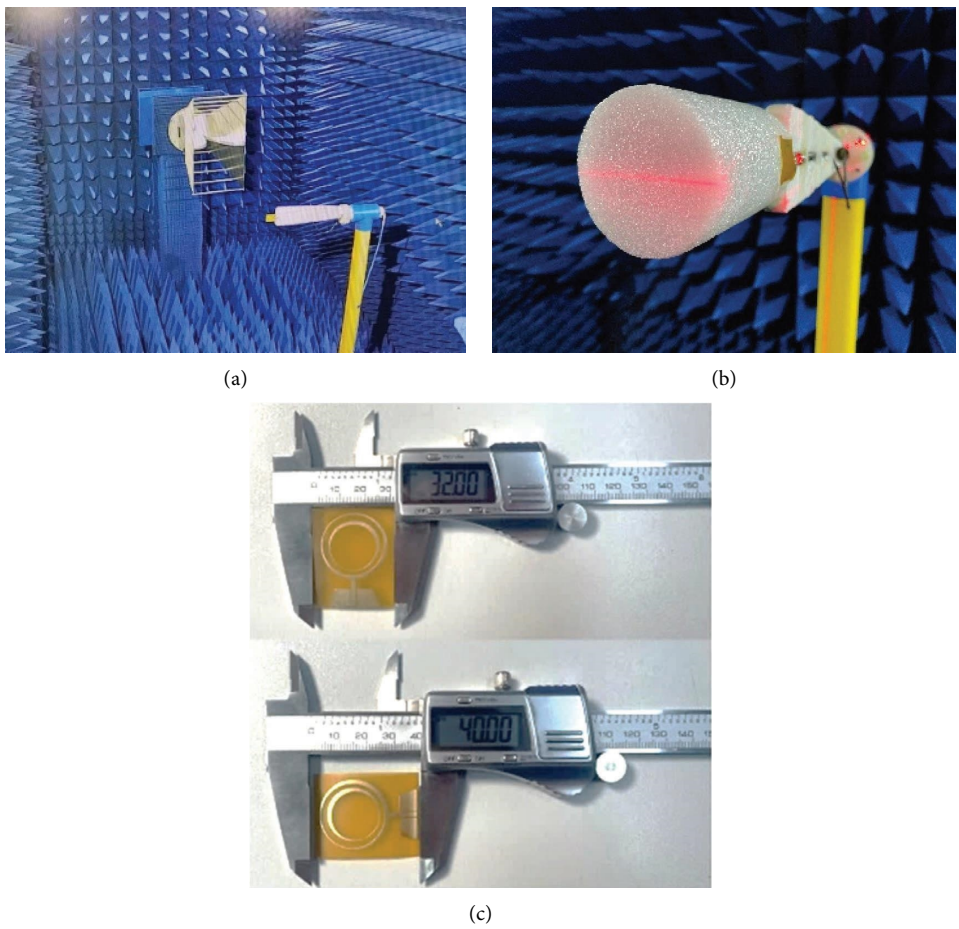

Figure 15: Test diagram of the antenna in an electromagnetic shielded darkroom. (a) Unbent, (b) curve, and (c) the antenna prototype.

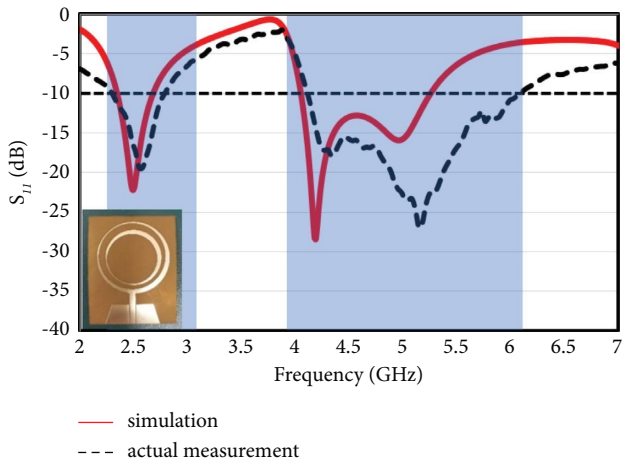

Figure 16: Comparison of S11 between actual measurement and simulation.

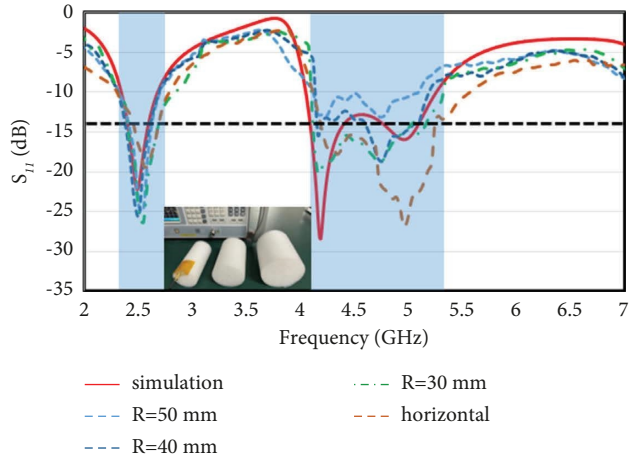

Figure 17: Comparison between antenna simulation and measurement of different curvatures.

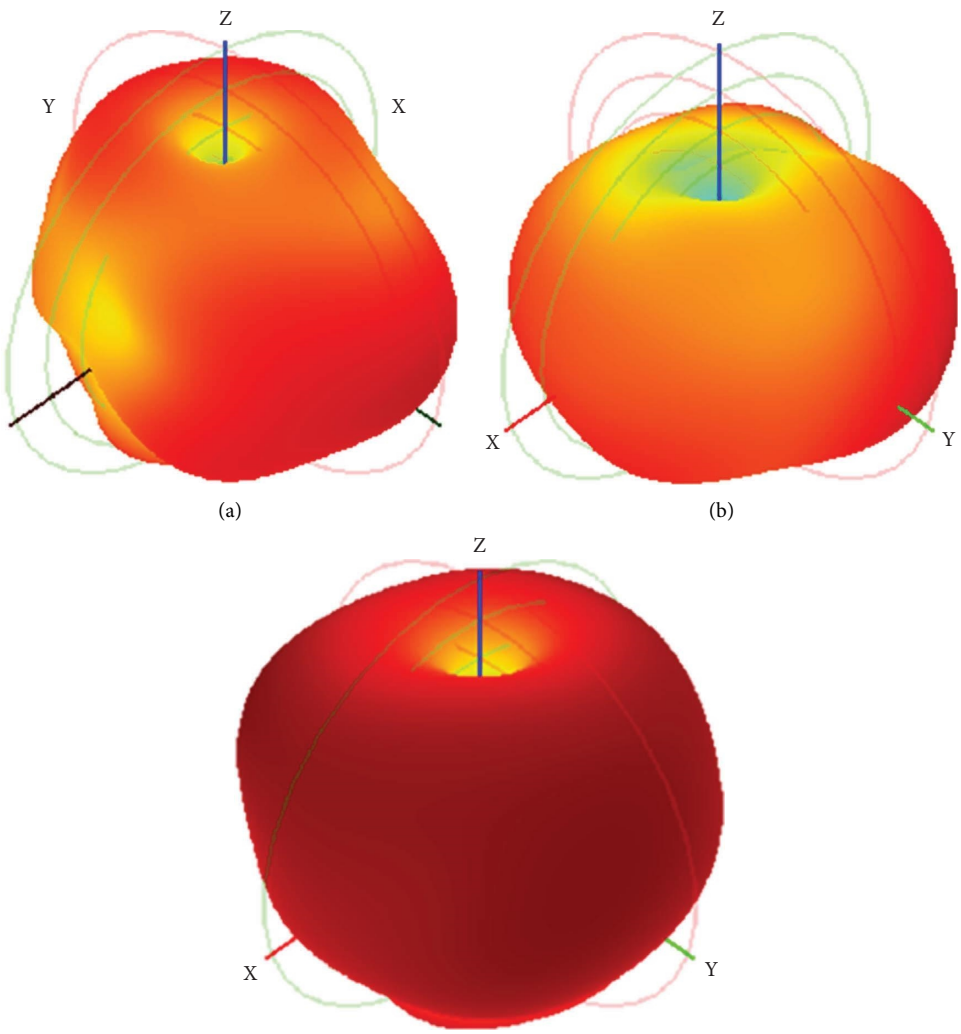

Figure 18: Antenna measurement 3D radiation pattern at (a) 2.489 GHz, (b) 4.189 GHz, and (c) 4.967 GHz.

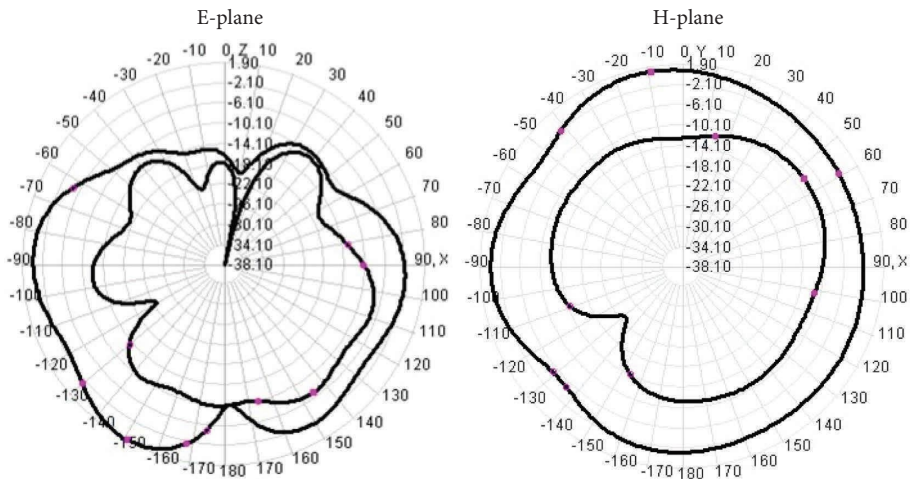

(a)

Figure 19: Continued.

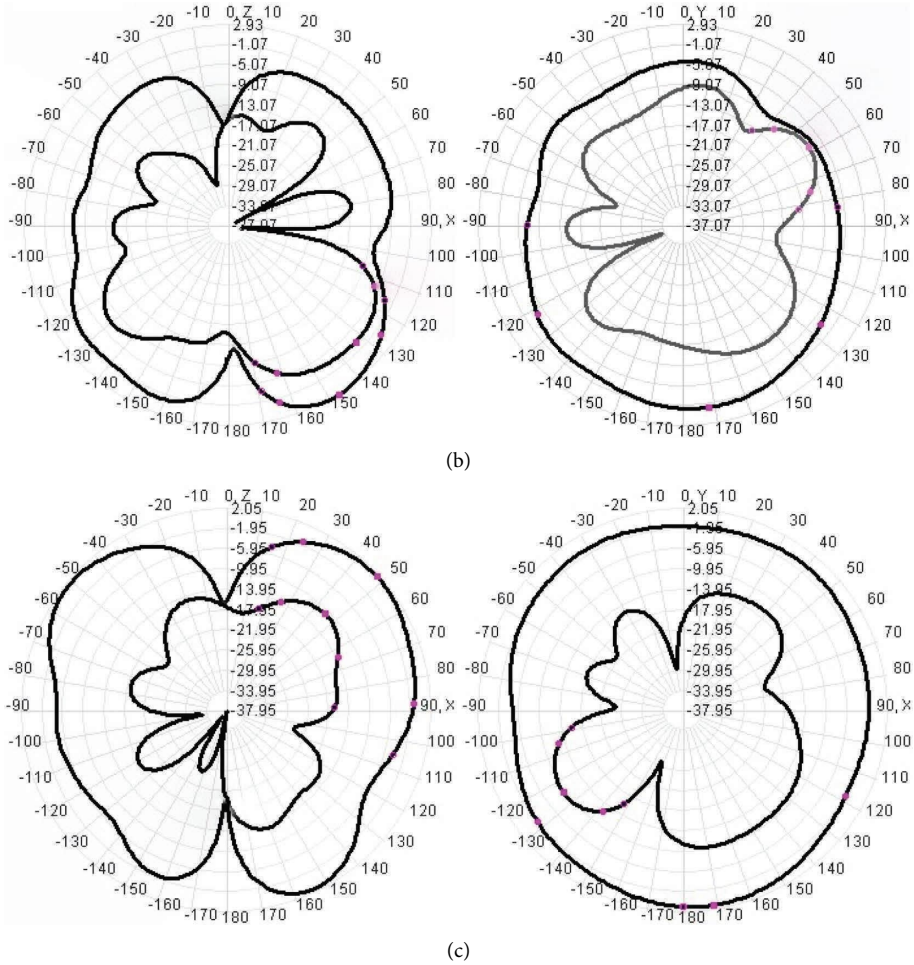

Figure 19: Cross-polarization of the E/H plane of the antenna at (a) 2.489 GHz, (b) 4.189 GHz, and (c) 4.967 GHz.

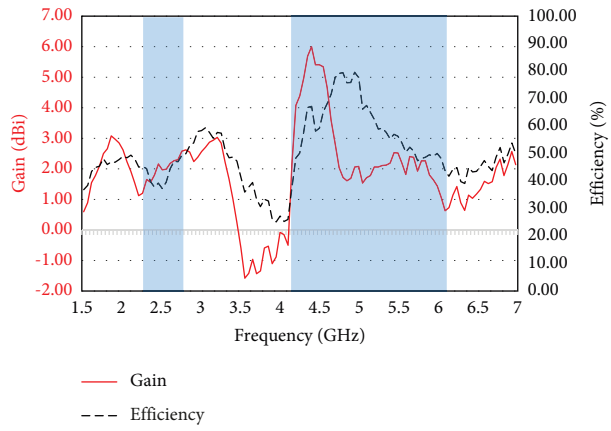

Figure 20: Gain and efficiency of antenna in the measured state.

3. Conclusion

In this paper, a small dual-band flexible antenna with an annular solar eclipse structure, measuring only $32 \times 40 \times 0.3\,\text{mm}^3$, was proposed. The final bands and bandwidths of the antenna are 2.32 GHz–2.78 GHz (19%) and 4.14 GHz–6.05 GHz (37%). The radiation of the antenna has good omnidirectionality, and the simulated and measured results are in good agreement, verifying the good radiation characteristics of the antenna. The flexible antenna has the characteristics of miniaturization, high stability, multifrequency band, and wearability. The antenna covers several commercial frequency bands such as the ISM2400 band, WLAN, WIMAX, and Bluetooth. The

antenna can be used in real-life industrial, scientific, and medical aspects.

Data Availability

The data used to support the results of this study are included in the Supplementary Information file and Figure files.

Conflicts of Interest

The authors declare that there are no conflicts of interest in this article.

Acknowledgments

This work was supported in part by the Natural Science Foundation of Hebei Province (No. F2021508009), the National Key R&D Project (No. 2020YFC1511805), the Fundamental Research Funds for the Central Universities (3142023058), and the Science and Technology Innovation for University Students Project Fund (0502010240-20).

References

[1] L. Song, A. C. Myers, J. J. Adams, and Y. Zhu, "Stretchable and reversibly deformable radio frequency antennas based on silver nanowires," *ACS Applied Materials and Interfaces*, vol. 6, no. 6, pp. 4248–4253, 2014.

[2] A. M. Hussain, F. A. Ghaffar, and S. I. Park, "Wearable electronics:Metal/polymer based stretchable antenna for constant frequencyfar-field communication in wearable electronics," *Advanced Functional Materials*, vol. 25, 2016.

[3] Z. Yan, T. Pan, G. Yao et al., "Highly stretchable and shapecontrollable three-dimensional antenna fabricated by Cut-Transfer-Release method," *Scientific Reports*, vol. 7, no. 1, Article ID 42227, 2017.

[4] P. Salonen, F. Yang, and Y. Rahmat-Samii, "WEBGA-wearable electromagnetic band-gap antenna," in *Proceedings of the IEEE Antennas and Propagation Society Symposium*, pp. 451–454, Monterey, CA, USA, June 2004.

[5] A. Pandya, T. K. Upadhyaya, and K. Pandya, "Tri-band defected ground plane based planar monopole antenna for Wi-Fi/WiMAX/WLAN applications," *Progress in Electromagnetics Research C*, vol. 108, pp. 127–136, 2021.

[6] A. Pandya, T. K. Upadhyaya, and K. Pandya, "Design of metamaterial based multilayer antenna for navigation/Wi-Fi/satellite applications," *Progress in Electromagnetics Research M*, vol. 99, pp. 103–113, 2021.

[7] A. Vahora and K. Pandya, "Implementation of cylindrical dielectric resonator antenna array for Wi-Fi/wireless LAN/satellite applications," *Progress in Electromagnetics Research M*, vol. 90, pp. 157–166, 2020.

[8] L. Liu, S. W. Cheung, and T. I. Yuk, "Compact MIMO antenna for portable devices in UWB applications," *IEEE Transactions on Antennas and Propagation*, vol. 61, no. 8, pp. 4257–4264, 2013.

[9] R. N. Tiwari, P. Singh, and B. K. Kanaujia, "A modified microstrip line fed compact UWB antenna for WiMAX/ISM/WLAN and wireless communications," *AEU-international journal of electronics and communications*, vol. 104, pp. 58–65, 2019.

[10] B. Kim, S. Nikolaou, and G. E. Ponchak, "A curvature CPW-fed ultra-wideband monopole antenna on liquid crystal polymer substrate using flexible characteristic," in *Proceedings of the IEEE Antennas and Propagation Society International Symposium*, pp. 1667–1670, Albuquerque, NM, USA, July 2006.

[11] J. N. Ramos-Silva, E. Ramírez-García, and B. A. Alcántara-Gavilan, "Design of acompact ultra wide band flexible antenna for personalmobile communications," in *Proceedings of the IEEE International Fall Meeting on Communications and Computing*, pp. 13–17, Acapulco, Mexico, March 2019.

[12] S. R. Zahran and M. A. Abdalla, "Novel flexible antennafor UWB applications," in *Proceedings of the IEEE International Symposium on Antennas and Propagation & USNC/URSI National Radio Science Meeting*, pp. 147-148, Vancouver, BC, Canada, July 2015.

[13] Z. Yu, G. Zhang, X. Ran, Z. Lin, and Y. Li, "A cloud-structured fractal multiband antenna for 4G/5G/WLAN/Bluetooth applications," *International Journal of Antennas and Propagation*, vol. 2022, Article ID 1270271, 10 pages, 2022.

[14] Z. Yu, G. Zhang, X. Ran et al., "Wearable portable flexible antenna covering 4G, 5G, WLAN, GPS applications," *Wireless Communications and Mobile Computing*, vol. 2023, Article ID 4667122, 11 pages, 2023.